



A Detailed Study of the Most Relaxed SPT-selected Galaxy Clusters: Properties of the Cool Core and Central Galaxy

M. McDonald¹, S. W. Allen^{2,3,4}, J. Hlavacek-Larrondo⁵ , A. B. Mantz^{2,3,4}, M. Bayliss¹ , B. A. Benson^{6,7,8}, M. Brodwin⁹ , E. Bulbul¹⁰, R. E. A. Canning^{2,3}, I. Chiu^{11,12,13}, W. R. Forman¹⁰ , G. P. Garmire¹⁴ , N. Gupta¹⁵, G. Khullar⁸ , J. J. Mohr^{12,13,16}, C. L. Reichardt¹⁵ , and T. Schrabback¹⁷

¹ Kavli Institute for Astrophysics and Space Research, Massachusetts Institute of Technology, 77 Massachusetts Avenue, Cambridge, MA 02139, USA
mcdonald@space.mit.edu

² Kavli Institute for Particle Astrophysics and Cosmology, Stanford University, 452 Lomita Mall, Stanford, CA 94305, USA

³ Department of Physics, Stanford University, 382 Via Pueblo Mall, Stanford, CA 94305, USA

⁴ SLAC National Accelerator Laboratory, 2575 Sand Hill Road, Menlo Park, CA 94025, USA

⁵ Département de Physique, Université de Montréal, C.P. 6128, Succ. Centre-Ville, Montréal, Québec H3C 3J7, Canada

⁶ Fermi National Accelerator Laboratory, Batavia, IL 60510-0500, USA

⁷ Kavli Institute for Cosmological Physics, University of Chicago, Chicago, IL 60637, USA

⁸ Department of Astronomy and Astrophysics, University of Chicago, Chicago, IL 60637, USA

⁹ Department of Physics and Astronomy, University of Missouri, 5110 Rockhill Road, Kansas City, MO 64110, USA

¹⁰ Harvard-Smithsonian Center for Astrophysics, 60 Garden Street, Cambridge, MA 02138, USA

¹¹ Academia Sinica Institute of Astronomy and Astrophysics, 11F of AS/NTU Astronomy–Mathematics Building, No.1, Section 4, Roosevelt Rd, Taipei 10617, Taiwan

¹² Faculty of Physics, Ludwig-Maximilians-Universität, Scheinerstr. 1, 81679 Munich, Germany

¹³ Excellence Cluster Universe, Boltzmannstr. 2, 85748 Garching, Germany

¹⁴ Huntingdon Institute for X-ray Astronomy, LLC, 10677 Franks Road, Huntingdon, PA 16652, USA

¹⁵ School of Physics, University of Melbourne, Parkville, VIC 3010, Australia

¹⁶ Max Planck Institute for Extraterrestrial Physics, Giessenbachstr. 1, 85748 Garching, Germany

¹⁷ Argelander-Institut für Astronomie, Auf dem Hugel 71, D-53121 Bonn, Germany

Received 2018 September 25; revised 2018 November 13; accepted 2018 November 21; published 2019 January 11

Abstract

We present a multi-wavelength analysis of the four most relaxed clusters in the South Pole Telescope 2500 deg² survey, which lie at $0.55 < z < 0.75$. This study, which utilizes new, deep data from the *Chandra X-ray Observatory* and *Hubble Space Telescope*, along with ground-based spectroscopy from Gemini and Magellan, improves significantly on previous studies in both depth and angular resolution, allowing us to directly compare to clusters at $z \sim 0$. We find that the temperature, density, and entropy profiles of the intracluster medium (ICM) are very similar among the four clusters, and share similar shapes to those of clusters at $z \sim 0$. Specifically, we find no evidence for deviations from self-similarity in the temperature profile over the radial range $10 \text{ kpc} < r < 1 \text{ Mpc}$, implying that the processes responsible for preventing runaway cooling over the past $\gtrsim 6 \text{ Gyr}$ are, at least roughly, preserving self-similarity. We find typical metallicities of $\sim 0.3 Z_{\odot}$ in the bulk of the ICM, rising to $\sim 0.5 Z_{\odot}$ in the inner $\sim 100 \text{ kpc}$, and reaching $\sim 1 Z_{\odot}$ at $r < 10 \text{ kpc}$. This central excess is similar in magnitude to what is observed in the most relaxed clusters at $z \sim 0$, suggesting that both the global metallicity and the central excess that we see in cool core clusters at $z \sim 0$ were in place very early in the cluster’s lifetime, and specifically that the central excess is not due to late-time enrichment by the central galaxy. Consistent with observations at $z \sim 0$, we measure a diversity of stellar populations in the central brightest cluster galaxies of these four clusters, with star formation rates spanning a factor of ~ 500 , despite the similarities in cooling time, cooling rate, and central entropy. These data suggest that, while the details vary dramatically from system to system, runaway cooling has been broadly regulated in relaxed clusters over the past 6 Gyr.

Key words: galaxies: clusters: general – galaxies: clusters: intracluster medium – galaxies: elliptical and lenticular, cD – X-rays: galaxies: clusters

1. Introduction

Galaxy clusters that are dynamically relaxed—defined based on either the dynamics and distributions of the member galaxies (e.g., Carlberg et al. 1997; Wen & Han 2013; Old et al. 2018) or the smoothness and symmetry of the X-ray-emitting intracluster medium (ICM; Mohr et al. 1993, 1995; Buote & Tsai 1995; Jeltema et al. 2005; Nurgaliev et al. 2013; Rasia et al. 2013; Mantz et al. 2015)—tend to have very uniform properties. These relaxed clusters, also commonly referred to as “cool core clusters,” have uniform density and temperature profiles (e.g., Vikhlinin et al. 2006; Baldi et al. 2012b; Mantz et al. 2016), with the temperature dropping by a factor of ~ 2 interior to $\sim 0.15 R_{500}$ (e.g., Vikhlinin et al. 2006). They have metallicity profiles with

peak values of $\sim 0.5\text{--}1.0 Z_{\odot}$ at their centers (e.g., De Grandi & Molendi 2001; Baldi et al. 2007; Leccardi & Molendi 2008; Mernier et al. 2016; Mantz et al. 2017), and reach a minimum of $\sim 0.2 Z_{\odot}$ outside the core (e.g., Baldi et al. 2012a; Werner et al. 2013; McDonald et al. 2016b; Ezer et al. 2017; Mantz et al. 2017; Mernier et al. 2017). These clusters tend to have a single massive galaxy at the center (e.g., Haarsma et al. 2010; Rossetti et al. 2016), referred to as the brightest cluster galaxy (BCG) or the central cluster galaxy. This massive galaxy is almost always radio-loud (e.g., Dunn & Fabian 2006; Sun 2009) and is often forming stars at a level far lower than would be implied by predictions based on the cooling rate of the ICM (e.g., O’Dea et al. 2008; McDonald et al. 2018).

It is unclear when each of these properties of relaxed clusters was established. There is some evidence that the thermodynamic profiles have evolved self-similarly since at least $z \sim 1$ (Baldi et al. 2012b; Mantz et al. 2016), that the metallicity peaks were in place early (Ettori et al. 2015; McDonald et al. 2016b; Mantz et al. 2017), and that the central active galactic nuclei (AGN) were already radio-loud ~ 6 Gyr ago (Hlavacek-Larrondo et al. 2012, 2015). However, much of our understanding of how galaxy clusters evolve is based on much shallower data than the depths that we routinely reach at $z \sim 0$. Specifically, X-ray observations of galaxy clusters at $z \sim 0$ have, on average, $>100,000$ counts, while those at $z \sim 1$ have ~ 2000 . In the optical, a typical ground-based observation of a galaxy cluster at $z \sim 0$ has a physical resolution of <1 kpc, while at $z \sim 1$ the resolution is nearly an order of magnitude worse. This can complicate analyses and make it difficult to directly compare systems over a large redshift range.

In this work, we attempt to even the playing field, providing deep *Chandra* and high-resolution *Hubble* observations in the X-ray and optical, respectively, to provide our first high-fidelity view of a sample of massive, relaxed clusters at $z \sim 0.7$. The goal of this work is to establish the properties of the most relaxed clusters in a mass-selected sample of high- z clusters, using data of similar quality to that obtained for low- z clusters. Specifically, we focus on the properties of the cluster core (thermodynamics, metallicity) and the central galaxy (morphology, stellar populations). We defer an analysis of the dynamical state of these clusters and the properties of their central AGNs to a companion paper. In Section 2 we define the sample, which is drawn from the South Pole Telescope (SPT) 2500 deg² SPT-SZ survey (Bleem et al. 2015), and describe the acquisition, reduction, and analysis of the X-ray and optical data. In Section 3 we present the results of this analysis, focusing on the thermodynamic profiles, the metallicity profiles, and the stellar populations of the central galaxy. In Section 4 we discuss these results, focusing on understanding the connection between the ICM and the central galaxy, and on understanding the lack of evolution in the metallicity profile. We finish in Section 5 with a summary of this work, and a look toward the future. Throughout this work, we assume $H_0 = 70 \text{ km s}^{-1} \text{ Mpc}^{-1}$, $\Omega_M = 0.3$, and $\Omega_\Lambda = 0.7$. Unless otherwise stated, error bars represent 68% confidence intervals.

2. Data and Analysis

2.1. Sample Selection

This sample of four clusters was drawn from the larger SPT-*Chandra* sample of 100 galaxy clusters, which were selected via the Sunyaev–Zel’dovich effect (Sunyaev & Zeldovich 1972) by the SPT, and then followed up to a common depth (~ 2000 counts) with *Chandra* (see, e.g., McDonald et al. 2013b, 2017). Of these 100 clusters, there are four that satisfy the conservative “relaxed” criterion, as described in Mantz et al. (2015): SPT-CLJ0000-5748, SPT-CLJ2043-5035, SPT-CLJ2331-5051, and the Phoenix cluster (hereafter SPT-CLJ2344-4243). These clusters are all found to have a centrally peaked surface brightness profile, with the peak centered on the large-scale X-ray centroid, and with isophotal ellipses that do not vary strongly in position angle (see Mantz et al. 2015 for a further description of this selection). All four of these clusters also satisfy the relaxation criterion of Nurgaliev et al. (2017), $A_{\text{phot}} < 0.2$, which (based on simulations) corresponds to

clusters that have not experienced a major merger in $\gtrsim 3$ Gyr. The most relaxed of these systems, SPT-CLJ2344-4243 (Phoenix), has been the subject of numerous studies (e.g., McDonald et al. 2012, 2013a, 2014b, 2015), and may be a rare example of runaway cooling in the ICM. Here, we present follow-up, multi-wavelength observations of these four relaxed clusters, which all have strong cool cores (McDonald et al. 2013a), evidence for strong radio-mode AGN feedback (Hlavacek-Larrondo et al. 2015), and star-forming central galaxies (McDonald et al. 2016a), similar to their low- z counterparts (e.g., McDonald et al. 2018). For each of these clusters, we have obtained deep *Chandra* and *Hubble Space Telescope* (*HST*) data, along with ground-based spectroscopy, in order to assess in greater detail the properties of the strongest cool cores as they were 6 Gyr ago.

2.2. Chandra X-Ray Data

X-ray observations for each of the four clusters in our sample were initially obtained as part of the larger SPT-*Chandra* survey (OBSIDs: 9333, 9335, 13401, 13478; PIs: Garmire, Benson). These initial observations yielded ~ 2000 counts per cluster, which was sufficient to determine their global metallicity (McDonald et al. 2016b), gas fraction (Chiu et al. 2016, 2018), whether they had a cool core (McDonald et al. 2013b), their dynamical state (Mantz et al. 2015; Nurgaliev et al. 2017), and to provide tentative detections of X-ray cavities in their core (Hlavacek-Larrondo et al. 2015). These clusters were then followed up with *Chandra* to reach count levels of $\sim 10,000$ (OBSIDs: 16135, 16545, 18238, 18239, 18240, 18241, 19695, 19697; PIs: McDonald, Hlavacek-Larrondo). To achieve these count levels, we required 218 ks (SPT-CLJ0000-5748), 189 ks (SPT-CLJ2043-5035), 151 ks (SPT-CLJ2331-5051), and 131 ks (SPT-CLJ2344-4243).

All *Chandra* data were reduced using CIAO v4.9 and CALDB v4.7.7. For each cluster, we reprocess the data using *chandra_repro*, cleaning the ACIS background in “very faint” mode. Point sources were identified using an automated routine following a wavelet decomposition technique (Vikhlinin et al. 1998), and then visually inspected before masking. Each OBSID was filtered for flares using the ChIPS routine *lc_clean*, and blank-sky background files were obtained using the *blanksky* routine. Background files were renormalized in the 10–12 keV bandpass (at which energies the effective area of *Chandra* is negligible) to match each observation. In addition to the blank-sky background, we extract an off-source spectrum for each observation at a physical distance of >3 Mpc from the cluster center, allowing us to better constrain the astrophysical background on an exposure-by-exposure basis.

We extract X-ray spectra in concentric annuli centered on the X-ray peak, using two separate binnings, one fine and one coarse. The coarse binning has sufficient width to provide $\gtrsim 2000$ counts per bin, allowing the measurement of spectroscopic quantities such as temperature and metallicity. These spectra are modeled in XSPEC v12.9.0¹⁸ (Arnaud 1996) over the energy range 0.7–7.0 keV using a combination of Galactic photoelectric absorption (PHABS), an optically thin plasma to represent the ICM (APEC), and two background components consisting of Galactic emission (APEC, $kT = 0.18$ keV,

¹⁸ APEC normalizations have been corrected for a known bug that leads to underestimates of densities by a factor of $(1+z)$ (<https://heasarc.gsfc.nasa.gov/docs/xanadu/xspec/issues/archive/issues.12.9.0u.html>).

$Z = Z_\odot$, $z = 0$) and unresolved point sources (BREMSS; $kT = 40$ keV). The two background components are joint-fit to the on-source and off-source spectra, with their normalizations per unit area tied between regions. When measuring spectroscopic temperature and metallicity for SPT-CLJ2344-4243, we mask the inner 2.5, which is contaminated by a strong central point source.

We also extract spectra in finely spaced annuli, starting at 1'' in width and growing as needed to be signal-dominated, for the purpose of measuring the emission measure profile. When modeling these spectra, we freeze the temperature and metallicity of the ICM to the values interpolated from the coarse temperature profile. This allows us to reduce the degrees of freedom in the fit, and constrain the density profile with much higher resolution. For the inner 2.5 of SPT-CLJ2344-4243, which is heavily contaminated by a central point source, we consider only energies < 2 keV. These energies are free from emission from the highly obscured (type-II) central QSO (Ueda et al. 2013), and this narrow energy band is sufficient to constrain a single free model parameter (normalization). We convert from the APEC normalization to emission measure using $\int n_e n_p dV = N \times 4\pi \times 10^{14} [D_A(1+z)]^2$, where N is the APEC normalization and D_A is the angular diameter distance to the cluster.

Emission measure profiles were fit by numerically integrating the three-dimensional density profile along the line of sight and over the width of each annulus, producing a projected profile. We assume that the three-dimensional profile is of the form described by Vikhlinin et al. (2006):

$$n_p n_e = n_0^2 \frac{(r/r_c)^{-\alpha}}{(1 + r^2/r_c^2)^{3\beta-\alpha/2}} \frac{1}{(1 + r^\gamma/r_s^\gamma)^{\epsilon/\gamma}} + \frac{n_{0,2}^2}{(1 + r^2/r_c^2)^{3\beta_2}}, \quad (1)$$

where we leave all parameters free except for γ , which is fixed to $\gamma = 3$, following Vikhlinin et al. (2006). The projected profile is fit to the data using the MPFITFUN procedure in IDL. We fit 100 realizations of the data, where data points are allowed to vary between fits based on their uncertainties, which provides an uncertainty in the fit. To convert from $n_e n_p$ to n_e , we assume $n_e = \sqrt{n_e^2} = \sqrt{1.199 n_e n_p}$, where $Z = n_e/n_p = 1.199$ is the average nuclear mass for a plasma with $0.3 Z_\odot$ metallicity, assuming abundances from Anders & Grevesse (1989).

The temperature profiles, which have between seven and nine radial bins, are fit using the MPFITFUN procedure in IDL with a modified version of the model from Vikhlinin et al. (2006):

$$T(r) = T_0 \frac{(r/r_{\text{core}})^\alpha + T_{\text{min}}/T_0}{(r/r_{\text{core}})^\alpha + 1} \frac{1}{1 + (r/r_{\text{out}})^2}. \quad (2)$$

This profile only has five free parameters, whereas the more general profile from Vikhlinin et al. (2006) has nine. We project this three-dimensional temperature model along the line of sight, and over the width of each bin, using our model density profile from above and assuming that

$$\langle T \rangle = \frac{\int_V w T dV}{\int_V w dV}, \quad (3)$$

where

$$w = n_e^2 T^{-0.75}, \quad (4)$$

following Vikhlinin (2006). This projected model was fit to the data, again using MPFITFUN and bootstrapping over 500 realizations of the temperature profile to provide uncertainties on the model.

In Table 1, we summarize some of the relevant X-ray properties for each cluster. We include the total mass M_Δ measured within R_Δ , the radius within which the average enclosed density is Δ times the critical density, where $\Delta = 500$ or 2500. These estimates are calculated from the pressure ($P \equiv n_e kT$) profile, assuming hydrostatic equilibrium. The estimates of M_{500} are poorly constrained due to the large uncertainties in the temperature model at $\gtrsim 0.5$ Mpc, so we also quote M_{500} from the Y_X - M scaling relation (Vikhlinin et al. 2009)—throughout this work, quoted R_{500} values will be derived from this scaling relation rather than from hydrostatic masses. We also include in this table the classical cooling rate ($\dot{M}_{\text{cool}} \equiv \frac{M_g(< r_{\text{cool}})}{t_{\text{cool}}}$, following McDonald et al. 2018), the central entropy ($K \equiv kT n_e^{-2/3}$), the central cooling time ($t_{\text{cool}} \equiv \frac{3}{2} \frac{(n_e + n_p) kT}{n_e n_H \Lambda(kT, Z)}$), and the average metallicity of the ICM in the inner (0.0–0.1 R_{500}) and outer (0.1–0.5 R_{500}) parts of the cluster. With the exception of the metallicities, which come from the spectral fitting, these are all derived directly from the three-dimensional density and temperature profiles, described above.

2.3. Optical Imaging

SPT-CLJ0000-5748 and SPT-CLJ2331-5051 were observed with *HST*/ACS as part of program GO 12246 (PI: Stubbs) between 2011 September 29 and November 27 using a single central pointing in F814W and a 2×2 mosaic in F606W. Each pointing was observed for 1.92 ks split into four exposures to facilitate removal of cosmic rays. For these clusters we employ the reduction described in Schrabback et al. (2018), which uses the algorithm of Massey et al. (2014) for the pixel-level correction for the impact of charge transfer inefficiency, CALACS for basic image reductions, scripts from Schrabback et al. (2010) for the image registration and weight optimization, and MultiDrizzle (Koekemoer et al. 2003) for the removal of cosmic rays and stacking.

We reduced *HST*/ACS observations of SPT-CLJ2043-5035 using the same pipeline, combining 2×2 mosaics obtained between 2015 October 20 and 25 in both F814W (1.96 ks per pointing) and F606W (1.93 ks per pointing) via program GO 14352 (PI: Hlavacek-Larrondo) with central single-pointing F606W observations (1.44 ks) obtained on 2014 May 24 via program SNAP 13412 (PI: Schrabback). For all three clusters, the two available filters span the 4000 Å break, providing a spatially resolved view of both the old and young stellar populations in the central BCG for each system.

SPT-CLJ2344-4243 was observed with WFC3-UVIS as part of the *HST* program GO 13102 (PI: McDonald) at F625W and F814W. Details of these data and their analysis are presented in McDonald et al. (2013a). These data are shallower than for the

Table 1
X-ray Properties of Relaxed SPT-selected Clusters

Cluster Name	z	$M_{500,HE}$ ($10^{14} M_{\odot}$)	M_{500,Y_X} ($10^{14} M_{\odot}$)	$M_{2500,HE}$ ($10^{14} M_{\odot}$)	R_{2500} (kpc)	\dot{M}_{cool} ($M_{\odot} \text{ yr}^{-1}$)	K_0 (keV cm^{-2})	$t_{cool,0}$ (Gyr)	$Z_{0.0-0.1}$ (Z_{\odot})	$Z_{0.1-0.5}$ (Z_{\odot})
SPT-CLJ0000-5748	0.7019	$9.7^{+5.9}_{-4.8}$	$4.1^{+0.7}_{-0.6}$	$2.1^{+0.5}_{-0.4}$	408^{+29}_{-24}	401 ± 30	11^{+3}_{-2}	$0.21^{+0.03}_{-0.03}$	$0.58^{+0.09}_{-0.08}$	$0.27^{+0.09}_{-0.09}$
SPT-CLJ2043-5035	0.7234	$9.3^{+4.2}_{-3.3}$	$4.2^{+0.1}_{-0.2}$	$1.5^{+1.2}_{-0.2}$	360^{+81}_{-21}	630 ± 56	12^{+3}_{-3}	$0.21^{+0.03}_{-0.04}$	$0.44^{+0.05}_{-0.05}$	$0.28^{+0.07}_{-0.07}$
SPT-CLJ2331-5051	0.5760	$6.8^{+2.1}_{-1.7}$	$4.3^{+0.3}_{-0.4}$	$2.6^{+0.8}_{-0.5}$	461^{+44}_{-30}	294 ± 24	15^{+5}_{-5}	$0.32^{+0.06}_{-0.08}$	$0.49^{+0.08}_{-0.08}$	$0.15^{+0.05}_{-0.06}$
SPT-CLJ2344-4243	0.5970	$13.5^{+3.6}_{-2.7}$	$14.3^{+0.8}_{-0.9}$	$6.3^{+0.8}_{-0.8}$	613^{+26}_{-27}	2366 ± 60	16^{+2}_{-3}	$0.18^{+0.01}_{-0.02}$	$0.47^{+0.04}_{-0.03}$	$0.39^{+0.06}_{-0.07}$

Note. Masses are calculated assuming hydrostatic equilibrium (HE) and the Y_X – M relation from Vikhlinin et al. (2009). Central quantities (K_0 , $t_{cool,0}$) are measured at a radius of 5 kpc. Metallicities are measured in annuli of 0.0–0.1 R_{500} and 0.1–0.5 R_{500} , following Mantz et al. (2017), where R_{500} is based on the Y_X – M relation. A description of these parameters, and how they were derived, can be found in Section 2.2.

other three clusters, but are sufficient for the purposes of this study, particularly because of the relative brightness of the central galaxy compared to other clusters.

Ground- and space-based broadband observations spanning rest-frame 0.1–13 μm were acquired for each BCG from McDonald et al. (2016a). Details of the data acquisition are presented therein. We use CIGALE¹⁹ (Burgarella et al. 2005) to estimate the stellar mass based on the spectral energy distribution (SED) and the intrinsic extinction due to dust for each BCG. The combination of rest-frame UV data (observed u -band) and mid-IR data from *WISE* provides strong constraints on the total stellar mass and the amount of intrinsic extinction—if the UV light is suppressed by extinction, we expect strong mid-IR emission; if there is no mid-IR emission, we expect the UV emission to be relatively unextincted. For all four BCGs we include an old and a young stellar population, attenuation and emission due to dust, and nebular lines due to warm ionized gas. For these fits, we assume extinction according to Calzetti et al. (1994), dust emission described by Dale et al. (2014), a Salpeter (1955) initial mass function, and a grid of old (4, 8, 12 Gyr) populations, starburst delay times (10, 20, 40, 80, 160, 320, 640 Myr), e -folding times (50, 250, 500, 1000, 2000, 4000, 6000, 8000 Myr), metallicities (0.004, 0.02, 0.05), and reddening ($E(B - V) = 0.0, 0.2, 0.4, 0.6$ mag). We include an AGN component for the BCG in SPT-CLJ2344-4243 based on photometric and spectroscopic observations in the UV–optical–IR (see, e.g., McDonald et al. 2015)—for the other three clusters there is no supporting evidence for an optical–IR bright nucleus, and the inclusion of an AGN weakens the constraints. We note that these estimates are based on aperture photometry (to avoid source confusion), with no attempt made to model the contribution to the total luminosity from large radii (i.e., intracluster light).

The results of this analysis for SPT-CLJ2043-5035, as an example, are shown in Figure 1, and for all four systems in Table 2. As is shown in Figure 1, the data in both the u -band and *WISE* W3 and W4 (upper limits) bands provide joint constraints on the total (observed and unobserved) mass of the youngest stellar populations.

2.4. Gemini/Magellan Optical Spectroscopy

Long-slit optical spectra for the central BCGs in SPT-CLJ0000-5748, SPT-CLJ2043-5035, and SPT-CLJ2344-4243 were obtained as a part of dedicated multi-slit observing campaigns to measure the redshifts of dozens of cluster member galaxies. The BCGs in SPT-CLJ0000-5748 and

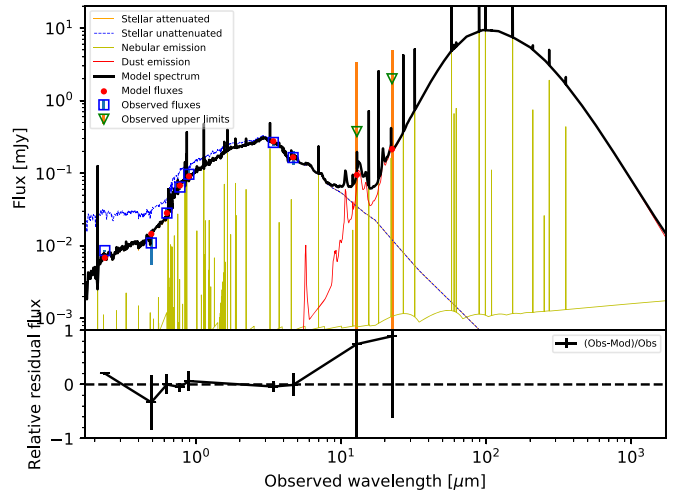


Figure 1. Rest-frame UV-through-IR SED for SPT-CLJ2043-5035. This SED, which was presented in McDonald et al. (2016a), has been fit using the CIGALE code, as described in Section 2.3. For all four BCGs in this paper, the CIGALE fits provide constraints on the total stellar mass of the old and young populations, along with the amount of intrinsic extinction due to dust within the system. The best-fit model is shown in black, but we note that we consider the range of allowable models in this analysis in order to fold the uncertainty on the extinction into estimates of the (for example) intrinsic [O II] luminosity.

SPT-CLJ2344-4243 were observed with the Gemini Multi-Object Spectrograph (GMOS; Hook et al. 2004) on the Gemini South telescope in 2010 September (GS-2009B-Q-16) and 2011 November (GS-2011A-C-3), respectively. The BCG in SPT-CLJ2043-5035 was observed with the Focal Reducer and low dispersion Spectrograph (Appenzeller et al. 1998, FORS2) on the Very Large Telescope in 2011 August as a part of ESO program 087.A-0843. The BCG in SPT-CLJ2331-5051 was observed with the Inamori-Magellan Areal Camera & Spectrograph (IMACS; Dressler et al. 2011) on the Magellan-I (Baade) telescope in 2017 December in long-slit mode as part of a dedicated program targeting BCGs. Spectra for all of these BCGs have relatively low resolution ($\lambda/\Delta\lambda \sim 400$ –1000) and cover wavelength ranges spanning most of the red side of the optical ($\Delta\lambda \sim 5000$ –10000 Å), corresponding to rest-frame blue ($\Delta\lambda_{\text{rest}} \sim 3000$ –6000 Å), with the exception of SPT-CLJ2344-4243 for which the choice of grating meant that the data span rest-frame 3500–4500 Å. We reduced the data using standard IRAF routines, with the GMOS, FORS2, and IMACS data making use of IRAF packages provided by Gemini, ESO, and Magellan, respectively. For further details of the observing strategy and data reduction methodology, we refer the reader to Ruel et al. (2014).

¹⁹ <https://cigale.lam.fr/>

Table 2
Properties of the Central Brightest Cluster Galaxy

Cluster Name	α_{BCG} (deg)	δ_{BCG} (deg)	$\Delta_{\text{X-BCG}}$ (arcsec kpc $^{-1}$)	$M_{*,\text{BCG}}$ ($10^{11} M_{\odot}$)	$L_{[\text{O II}],\text{BCG}}$ ($10^{41} \text{ erg s}^{-1}$)	$E(B - V)_{\text{SED}}$	$\text{SFR}_{[\text{O II}],\text{BCG}}$ ($M_{\odot} \text{ yr}^{-1}$)	sSFR_{BCG} (Gyr^{-1})
SPT-CLJ0000-5748	0.2503	-57.8093	0.7/5.2	$12.4^{+1.3}_{-0.7}$	15.1 ± 0.9	$0.17^{+0.18}_{-0.13}$	$17.8^{+13.7}_{-6.2}$	$0.014^{+0.011}_{-0.005}$
SPT-CLJ2043-5035	310.8233	-50.5923	1.5/10.7	$4.1^{+0.0}_{-1.3}$	34.8 ± 0.9	$0.11^{+0.06}_{-0.04}$	$33.1^{+7.1}_{-4.6}$	$0.090^{+0.037}_{-0.017}$
SPT-CLJ2331-5051	352.9631	-50.8645	1.6/10.6	$9.3^{+3.1}_{-2.4}$	1.5 ± 1.2	$0.17^{+0.21}_{-0.13}$	$1.8^{+2.4}_{-1.4}$	$0.002^{+0.003}_{-0.001}$
SPT-CLJ2344-4243	356.1831	-42.7201	<0.5/<3.3	$14.5^{+0.8}_{-0.6}$	339.6 ± 10.6	$0.39^{+0.04}_{-0.05}$	$809.7^{+110.0}_{-116.4}$	$0.554^{+0.081}_{-0.082}$

Note. The BCG separation ($\Delta_{\text{X-BCG}}$) is the projected distance between the brightness peak of the galaxy identified as the BCG and the soft X-ray peak. Due to the highly clumpy morphology of the BCG in SPT-CLJ2344-4243, which makes the center challenging to identify, the quoted offset is considered to be an upper limit. Quoted $L_{[\text{O II}]}$ values are uncorrected for intrinsic extinction. Star formation rates (SFRs) and specific star formation rates (sSFR) are derived from the $[\text{O II}]$ flux and include combined uncertainty in the $[\text{O II}]$ flux, the intrinsic extinction ($E(B - V)$), and the stellar mass. Stellar masses and intrinsic extinction are derived based on the SED fit (see Section 2.3)—the former do not contain the extended cD envelope.

and Bayliss et al. (2016), in which most of these data were originally presented.

Some of the optical spectra used in this work are not flux-calibrated using spectrophotometric standards, because they were obtained with the intention of measuring redshifts, rather than fluxes. We use the 0.1–13 μm SEDs provided in McDonald et al. (2016a) to roughly estimate the flux calibration at four points (g , r , i , z) by convolving the uncalibrated spectrum with the filter bandpasses. This flux calibration is applied to the data, yielding the spectra shown in Figure 2. These spectra are not suitable for full spectral modeling, due to the fact that their shapes are poorly constrained by only four data points. Locally, the calibration should not vary greatly, so relative, local measurements such as the strength of the 4000 \AA break and equivalent width measurements of individual lines are relatively unaffected.

We use SED modeling of the broadband, flux-calibrated photometry described in Section 2.3 to estimate the flux at rest-frame 3727 \AA , which we then combine with local spectroscopic measurements of the $[\text{O II}]$ equivalent width to estimate the calibrated flux of the $[\text{O II}]$ emission line doublet. We correct for intrinsic absorption due to dust using the measured attenuation from the CIGALE SED model, along with the uncertainty in this measurement (see Table 2). When converting from the extinction-corrected $[\text{O II}]$ luminosity to star formation rate, we follow the prescriptions described in Kewley et al. (2004). Quantities extracted from these photometric and spectroscopic analyses are provided in Table 2 for each BCG.

3. Results

3.1. Thermodynamic Profiles and Central Properties

For each cluster, we have measured the emission measure and projected temperature profile from X-ray spectra, as described in Section 2.2. We model these profiles by projecting a three-dimensional model onto two dimensions, and then fitting the projected model to the data. We can then infer the analytic form of the three-dimensional temperature and density profiles, which can be used to infer the three-dimensional entropy, cooling time, and pressure (which is used to determine the hydrostatic mass).

In Figure 3, we show the results of this analysis. In the upper and lower panels, we show the projected emission measure and projected temperature profiles, respectively, along with the best-fit models and the 1σ uncertainty in these models. In all four clusters, the density profile is strongly peaked in the center, indicating the presence of a cool core. This is unsurprising—our sample was

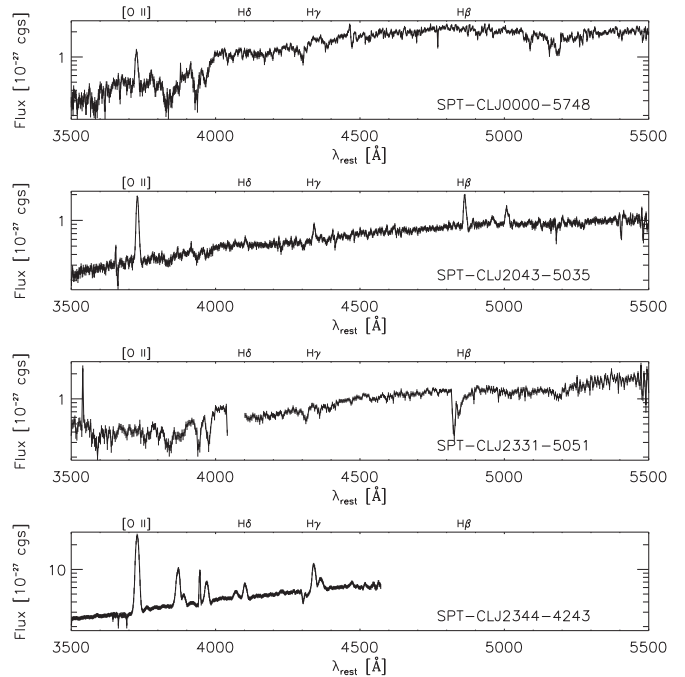


Figure 2. Optical spectra for the central, brightest cluster galaxy in each of our four clusters. These systems show a variety of features, including strong $[\text{O II}]$ emission (SPT-CLJ2043-5035, SPT-CLJ2344-4243), weak $[\text{O II}]$ emission (SPT-CLJ0000-5748), strong 4000 \AA breaks (SPT-CLJ0000-5748, SPT-CLJ2331-5051), and a variety of absorption lines (SPT-CLJ0000-5748, SPT-CLJ2331-5051). For the analysis presented in this work, we consider only the brightness and width of the $[\text{O II}]$ $\lambda\lambda 3726, 3729$ doublet relative to the nearby continuum. We note that data are missing in the spectrum for SPT-CLJ2331-5051 due to a chip gap, and the bright narrow line at ~ 3500 \AA is a residual sky line. For SPT-CLJ2344-4243 the choice of grating led to sensitivity at $\lambda_{\text{obs}} < 7350$ \AA only.

selected to contain the most relaxed, strongest cool cores in the full SPT-*Chandra* sample of 100 clusters. All four of these clusters satisfy density-based criteria for cool cores (see Semler et al. 2012; McDonald et al. 2013b), including the cuspieness ($\alpha \equiv \frac{d \log \rho_g}{d \log r} \Big|_{r=0.04 R_{500}} > 0.7$; Vikhlinin et al. 2007) and concentration ($C_{SB} \equiv \frac{F_X(r < 40 \text{ kpc})}{F_X(r < 400 \text{ kpc})} > 0.155$; Santos et al. 2008).

These density peaks are coincident with a significant drop in temperature at the cluster center. We find three-dimensional drops in central temperature (T_{min}/T_0 , see Equation (2)) of $0.17^{+0.12}_{-0.07}$, $0.23^{+0.19}_{-0.10}$, $0.15^{+0.14}_{-0.07}$, and $0.41^{+0.24}_{-0.15}$ for SPT-CLJ0000-5748, SPT-CLJ2043-5035, SPT-CLJ2331-5051, and SPT-CLJ2344-4243, respectively. For comparison,

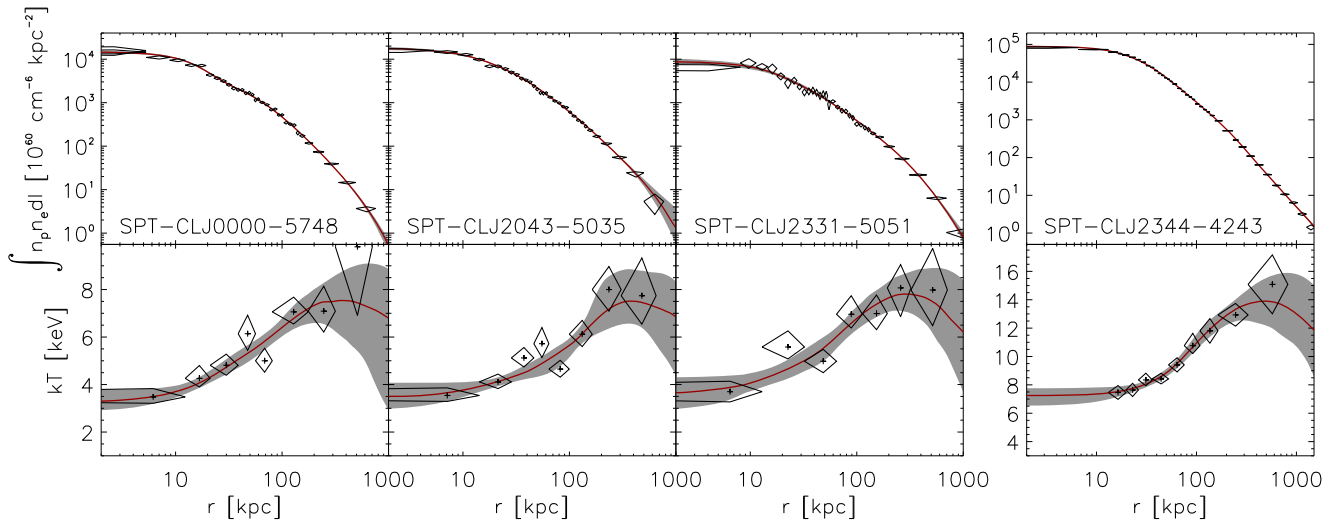


Figure 3. Thermodynamic profiles for all four clusters, as described in Section 2.2. We note that, since SPT-CLJ2344-4243 has a factor of ~ 2 higher mass than the other three systems, we have adjusted the plotting limits for the temperature and density profiles. Upper row: these panels show the emission measure profile for each of the clusters, with sampling chosen to produce a well-sampled profile with high signal-to-noise ratio. This projected profile is fit with a three-dimensional model (see Equation (1)), which has been projected along the line of sight and along the radial direction within each bin. All four clusters exhibit a central overdensity, indicative of a cool core. Lower row: these panels show the projected temperature profile, with a coarser sampling that reflects the added complexity of constraining the spectroscopic temperature and metallicity. These profiles have been fit with a three-dimensional model (see Equation (2)), which has been projected along the line of sight following Equation (3). All four clusters have similar temperature profiles, reaching a maximum projected temperature at ~ 300 kpc that is $\sim 2\times$ higher than the minimum projected temperature measured at ~ 10 kpc.

Vikhlinin et al. (2006) find T_{min}/T_0 ranging from 0.1 to 0.4 for the five most massive clusters in their sample of relaxed, low- z clusters. We find cool core sizes, as measured from the temperature profile (r_{core} , see Equation (2)), of 135–250 kpc for the four SPT clusters, compared to typical values of 30–214 kpc for the five most massive clusters from Vikhlinin et al. (2006). Relative to the measured values of R_{2500} , these core radii are, on average, larger for SPT clusters ($\sim 40\%$ of R_{2500}) than those from Vikhlinin et al. (2006) ($\sim 20\%$ of R_{2500}); however, both samples are too small to draw definitive conclusions. Overall, it appears that the temperature profiles in these four relaxed clusters at $z \sim 0.7$ share similar shapes to those at $z \sim 0$.

To further investigate the evolution of the three-dimensional density and temperature profiles, we compare to a similarly selected sample of relaxed clusters at $z < 0.3$ from Mantz et al. (2016). The four systems in this work satisfy the same conservative relaxation criteria (namely that they are centrally peaked, azimuthally symmetric, and well aligned) as the primarily X-ray-selected $z < 0.3$ clusters described in Mantz et al. (2015). In Figure 4 we show the individual three-dimensional profiles, scaled according to the self-similar model of Kaiser (1986) and as a function of scaled radius (R_{2500}). For both the density and temperature profiles, the SPT clusters lie within the 1σ loci defined by the $z < 0.3$ relaxed cluster sample (Mantz et al. 2016), implying that their evolution is well described by a self-similar model at all radii. The only exception to this is the core of the Phoenix cluster (SPT-CLJ2344-4243), which is the strongest known cool core and thus traces the high-density edge of the 2σ locus. The four SPT clusters appear to have shallower inner slopes in the temperature profiles (reaching maxima at larger radii), consistent with the overall larger core radii mentioned above. We note that this slower rise of the temperature profile is consistent with the picture presented in McDonald et al. (2017), where the cool core is a fixed physical size (corresponding to the “reach” of the central AGN) and the bulk of the cluster is

evolving self-similarly, leading to a decreasing ratio of the cool core to cluster size (R_{500}) with decreasing redshift. However, we show in the lower panel of Figure 4 that this is not statistically significant—all four clusters lie within the 1σ scatter for low- z clusters when we consider uncertainties on our temperature measurements. Further, we note that a $<5\%$ systematic offset between our estimates of R_{2500} and those of Mantz et al. (2016)—which is a completely realistic offset between two independent analyses and on par with the statistical uncertainty in R_{2500} —is sufficient to remove this slight discrepancy. Given these points, we would require significantly more than four clusters to claim any deviation from self-similarity in the temperature profiles of relaxed clusters.

All four clusters have very similar density and temperature profiles, which naturally leads to very similar entropy ($K \equiv kTn_e^{-2/3}$) profiles, as we show in Figure 5. At large radii, these profiles follow the expectation if gravity is the only relevant physics ($K \propto r^{1.2}$; Voit et al. 2005). We see no evidence for a flattening of the entropy profile at radii near R_{500} (~ 1 Mpc), as was seen for more distant ($z > 0.6$) clusters in McDonald et al. (2014a). At small radii ($r \lesssim 30$ kpc), we detect a significant entropy excess above the gravity-only prediction, leading to a shallower slope for all three clusters. This change in slope is consistent with what is observed at $z \sim 0$ (Cavagnolo et al. 2009; Panagoulia et al. 2014; Babyk et al. 2018), and is indicative of baryonic physics (i.e., cooling, feedback) beginning to play a significant role. Over the full radial range considered, the profiles are consistent (at the level of 1σ – 2σ) with the universal entropy profile for cool core clusters from Babyk et al. (2018). There is marginal ($\sim 2\sigma$) evidence for a dearth of entropy at ~ 30 – 100 kpc in SPT-CLJ2043-5035 and SPT-CLJ2344-4243, with these two profiles falling below the profiles of both Voit et al. (2005) and Babyk et al. (2018) at the $\sim 2\sigma$ level over this radial range. At radii smaller and larger than this intermediate region, the

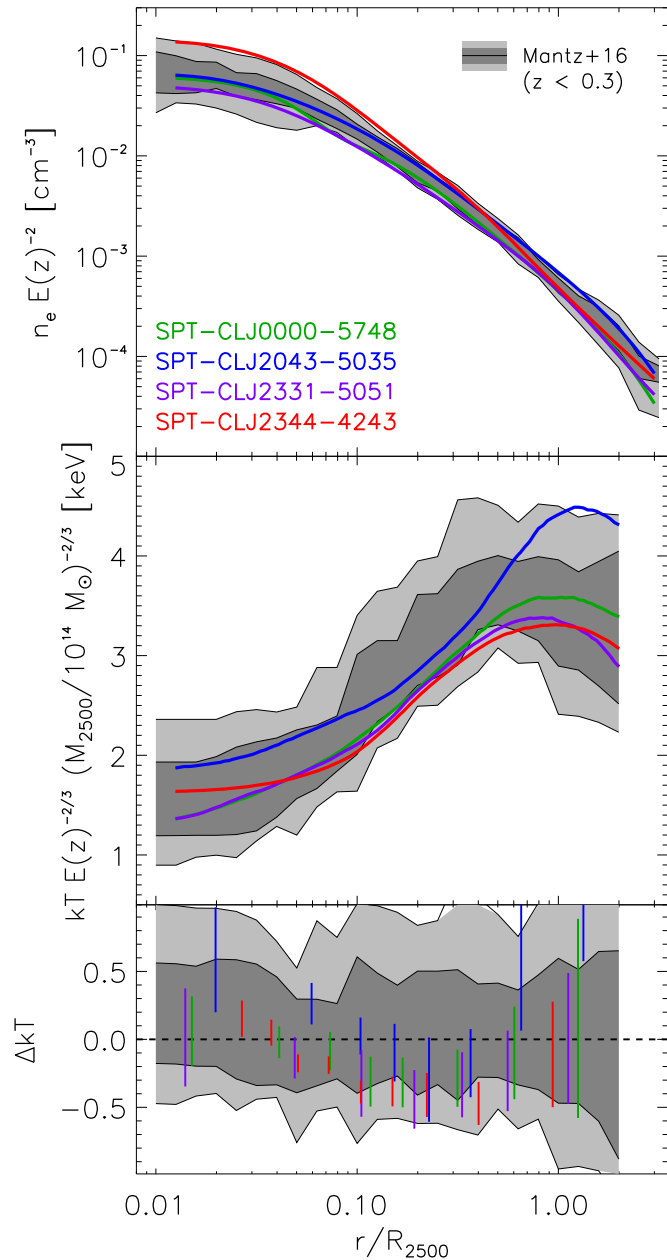


Figure 4. In all three panels, we compare the three-dimensional thermodynamic profiles for our four relaxed clusters to those of a similarly selected sample of relaxed clusters at $z < 0.3$ from Mantz et al. (2016). The latter are depicted as gray bands, with dark and light bands representing the 1σ and 2σ scatter. All profiles have been scaled according to the self-similar model of Kaiser (1986), and are plotted as a function of scaled radius (R_{2500}). In the lower panel, we show the residual between individual clusters in our sample and the average relaxed cluster at $z < 0.3$, demonstrating that, given the measurement uncertainty, all four clusters are consistent with self-similar evolution over the past 6 Gyr.

four profiles are statistically indistinguishable from one another.

We measure the central entropy for each cluster at a radius of 5 kpc, to avoid interpolating far beyond where our data can constrain. We find $K_0 = 11, 12, 15,$ and 16 keV cm^2 for SPT-CLJ0000-5748, SPT-CLJ2043-5035, SPT-CLJ2331-5051, and SPT-CLJ2344-4243, respectively. These are all within 1σ of the values quoted in McDonald et al. (2013b), where we were unable to constrain the temperature profile due to a lack of counts, and instead assumed a universal temperature profile

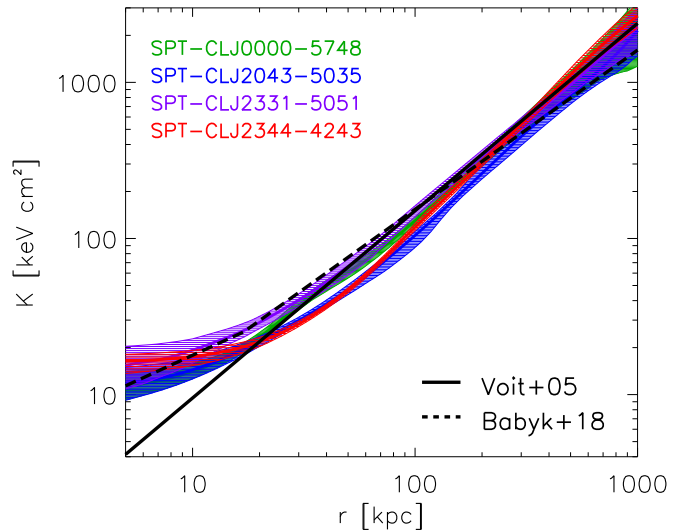


Figure 5. The three-dimensional entropy profile is computed combining the model three-dimensional temperature and density profiles ($K \equiv kTn_e^{-2/3}$). These profiles all agree well with one another, and with those from the literature, at large and small radii. We see a weak separation between “high-entropy” (SPT-CLJ0000-5748, SPT-CLJ2331-5051) and “low-entropy” (SPT-CLJ2043-5035, SPT-CLJ2344-4243) systems over the radial range 25–100 kpc, with the two groups merging at smaller and larger radii.

with a single free parameter. This demonstrates that, at least for the most relaxed clusters, such an approach is valid. The small scatter in central entropies for these systems suggests a relatively gentle feedback cycle—periods of runaway cooling and/or powerful AGN outbursts would act to increase the scatter in the central entropy for a sample of relaxed clusters. All four of these cluster cores lie below the entropy threshold for multiphase gas ($K_0 < 30 \text{ keV cm}^2$; Cavagnolo et al. 2008), implying that the central galaxies in these clusters ought to have strong $H\alpha$ emission and other signatures of star formation—we will return to this point in Section 3.3 and in the discussion.

3.2. Metallicity Profiles and Central Metallicity Peak

In Figure 6 we show the metallicity profiles for each cluster. We measure the metallicity in each bin for which we measure temperature (see Section 2.2), and separately in bins of $0.0\text{--}0.1 R_{500}$ and $0.1\text{--}0.5 R_{500}$, following Mantz et al. (2017). The latter measurements are quoted in Table 1. We assume solar abundances from Anders & Grevesse (1989) to be consistent with the bulk of the literature, but note that our metallicities can be roughly converted to those based on solar abundances from Asplund et al. (2009) by multiplying by a factor of 1.4. While not perfect, this multiplicative factor is accurate to better than our measurement uncertainties.

Figure 6 shows steeply rising metallicity profiles for three of the four clusters in our sample. Outside the innermost bin ($r \gtrsim 15 \text{ kpc}$) these metallicity profiles are all consistent at the 1σ level with the average profile for massive cool core clusters at $z \sim 0$ (De Grandi & Molendi 2001, not shown) and from $z = 0.1\text{--}0.3$ (Baldi et al. 2007). In the innermost bin ($r \lesssim 15 \text{ kpc}$), we find $Z \sim Z_\odot$ in all three systems for which such a measurement is possible, with large uncertainties. To test the statistical significance of these highly enriched central regions, we perform a somewhat unorthodox test. In the previous section, we have established how remarkably similar

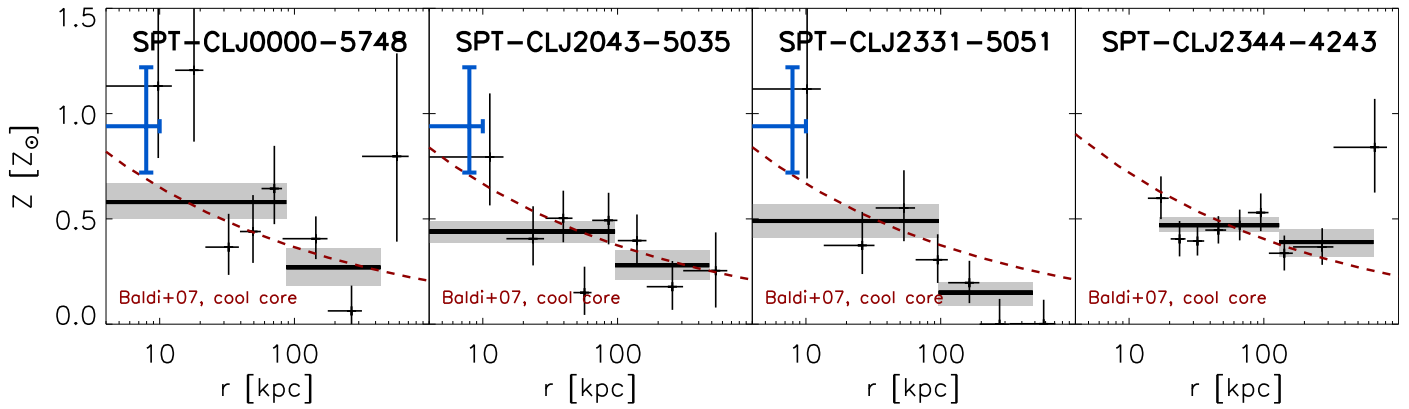


Figure 6. ICM metallicity profiles for the four clusters in our sample. Black crosses show the metallicity measured with the same sampling as the temperature profile (see Figure 3). We note that the inner 2°5 for SPT-CLJ2344-4243 has been masked due to contamination by a bright central X-ray point source with an Fe K α emission line of extremely high equivalent width. Thick black lines with gray boxes show the metallicity and its uncertainty measured in annuli of $0 < r < 0.1 R_{500}$ and $0.1 R_{500} < r < 0.5 R_{500}$, following Mantz et al. (2017). Blue points show the joint constraint on the metallicity in the inner 10 kpc from SPT-CLJ0000-5748, SPT-CLJ2043-5035, and SPT-CLJ2331-5051, assuming all three clusters have a shared temperature and metallicity (see Section 3.2 for more details). We compare these profiles to the average profile for low- z cool core clusters (red dashed line; Baldi et al. 2007), finding that the profiles agree well at all radii, with weak ($\sim 1\sigma$) evidence for a slightly higher than average central ($r < 10$ kpc) metallicity in the high- z clusters.

the thermodynamic profiles of these clusters are: in the inner ~ 10 kpc, all three of the lower-mass clusters (excluding SPT-CLJ2344-4243) have consistent temperatures, emission measures, entropies, and cooling times to within the 1σ uncertainties. For this reason, we feel comfortable combining these three systems into a single stacked cluster in order to improve the constraints on the metallicity. We have extracted spectra in the inner 10 kpc for all three clusters and fit them jointly with an APEC model for which we tie the metallicity and temperature, fix the column density and redshift to the nominal values, and allow the normalization (which is a function of distance) to vary. We find a combined central temperature of $3.67^{+0.26}_{-0.23}$ keV (consistent with Figure 3) and a combined metallicity of $0.94^{+0.28}_{-0.22} Z_{\odot}$ in the inner 10 kpc. These data points are shown in Figure 6 for comparison to the literature and the individual profiles. This central metallicity, which is a factor of $\sim 4\times$ higher than that measured in the bulk ($0.1\text{--}0.5 R_{500}$) of the four clusters, is higher than that measured at the same radii in Perseus (Schmidt et al. 2002), Hydra A, and A1835 (Kirkpatrick et al. 2011) and is consistent with some of the most metal-peaked clusters, including A262 (Kirkpatrick et al. 2011). Given that the metallicity profile should become cuspy with time, due to localized enrichment from the central galaxy, the fact that these three clusters at $\langle z \rangle \sim 0.7$ have slightly ($\sim 1\sigma$) overenriched cores compared to those from Baldi et al. (2007) may indicate that the process responsible for mixing gas (e.g., AGN feedback, sloshing of the cool core in the cluster potential) in the central part of the cluster was not operating as effectively 6 Gyr ago as it is today. This could mean that at early times mixing was suppressed, or that at late times it is enhanced.

While it has been well established that the bulk of the metals in the cluster ICM were formed early on (Werner et al. 2013; Etti et al. 2015; McDonald et al. 2016b; Mantz et al. 2017), relatively few studies have targeted the metal-enriched cores of cool core clusters, which are typically overabundant by $\Delta Z \sim 0.3 Z_{\odot}$ (De Grandi & Molendi 2001). Mantz et al. (2017) found no evolution ($\beta_{1+z} = -0.14 \pm 0.17$) in the core ($0.0\text{--}0.1 R_{500}$) metallicity of massive clusters spanning $0 < z < 1.2$, while McDonald et al. (2016b) find $dZ/dz = (-0.04 \pm 0.1 Z_{\odot})$ for the cores ($0.0\text{--}0.15 R_{500}$) of clusters

spanning $0.1 < z < 1.7$. Considering only cool core clusters, McDonald et al. (2016b) find $dZ/dz = -0.21 \pm 0.11 Z_{\odot}$, which was suggestive of mild evolution ($\sim 1/3$ of metals in core created since $z \sim 1$) in the core metallicity.

While this work is based on only four clusters, one of which is highly contaminated in the core due to the presence of a bright point source, it suggests that, for the most relaxed clusters, the central metal excess that we observe at $z \sim 0$ was already in place 6 Gyr ago. We will return to this in a discussion below.

3.3. Properties of the Central Galaxy

Relaxed, cool core galaxy clusters at $z \sim 0$ tend to have star-forming central galaxies (e.g., McNamara & O’Connell 1989; O’Dea et al. 2008; McDonald et al. 2018; Runge & Yan 2018) that are well aligned with the X-ray peak. This seems to be the case at higher redshift to the degree that it has been tested (e.g., Fogarty et al. 2015). Recent work (Webb et al. 2015; McDonald et al. 2016a; Bonaventura et al. 2017) has shown that, at $z \gtrsim 1$, clusters harbored central galaxies that were forming stars at rates of $\sim 100 M_{\odot} \text{ yr}^{-1}$, compared to typical rates of $1\text{--}10 M_{\odot} \text{ yr}^{-1}$ at $z \sim 0$ (O’Dea et al. 2008; McDonald et al. 2018). However, much of this high- z star formation appears to be fueled by gas-rich mergers, and is predominantly found in the centers of disturbed, non-cool core clusters. This study represents an opportunity to test, in the most relaxed clusters at $z \sim 0.7$, how much star formation can be attributed to cooling of the hot ICM.

In Figure 7, we show X-ray and optical images of the cluster (upper panels, 1 Mpc on a side), the central core (middle panels, 200 kpc on a side), and the central galaxy (lower panels, 50 kpc on a side). In all four clusters, there is a massive, giant elliptical galaxy nearly coincident with the X-ray peak. We find physical, two-dimensional offsets between the BCG and the X-ray peak of $\lesssim 3\text{--}10$ kpc (see Table 2). These small offsets are consistent with what is found in typical low- z cool core clusters ($\sim 3\text{--}10$ kpc; Sanderson et al. 2009), and indicate a relatively small degree of dynamical activity. SPT-CLJ2331-5051 and SPT-CLJ2344-4243 appear to harbor the most dominant central galaxy, with no other massive galaxies within the inner ~ 100 kpc of the cluster center. SPT-CLJ0000-5748 has a close,

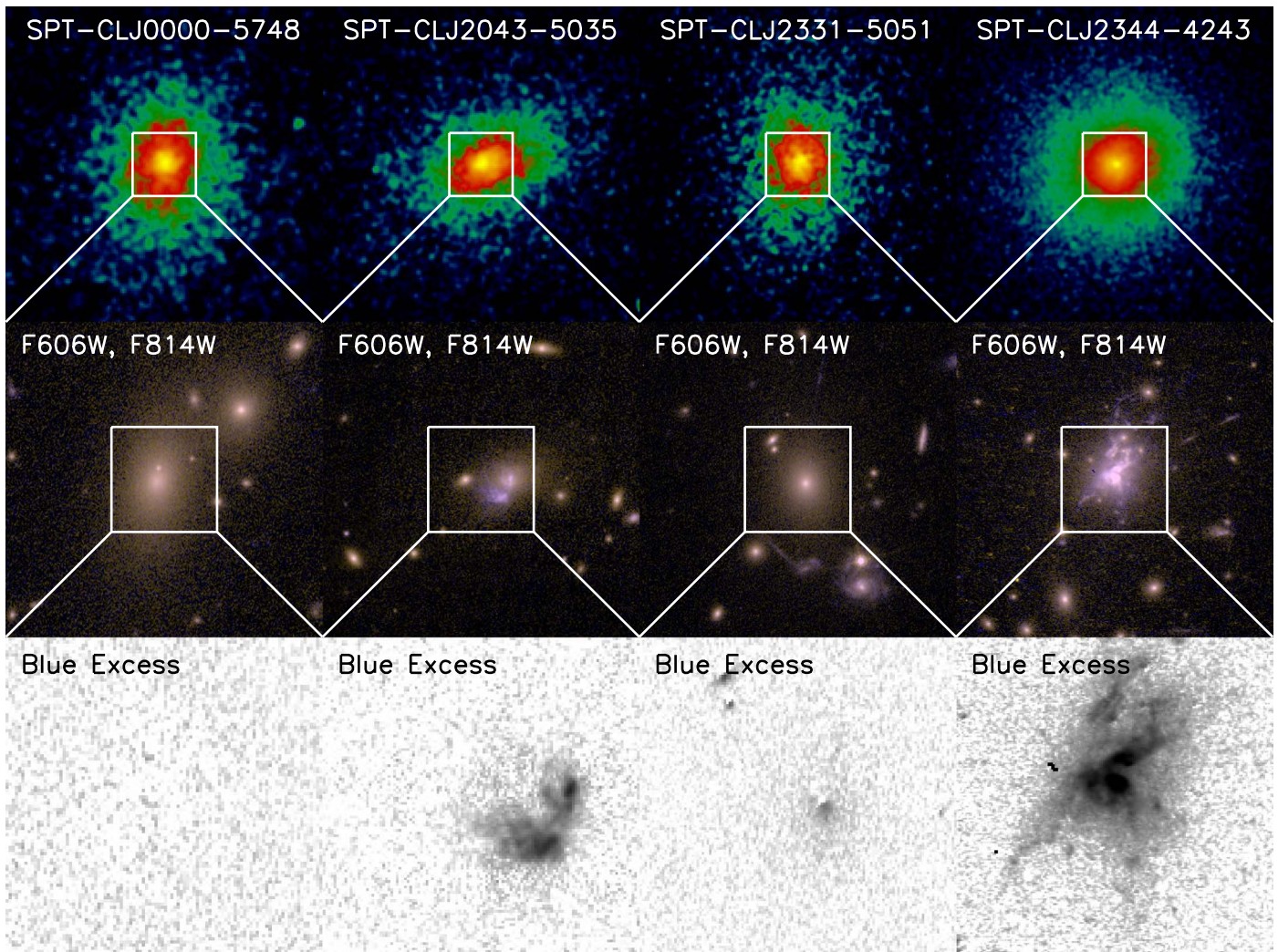


Figure 7. Upper row: X-ray image (0.7–4.0 keV) of each cluster, showing the relatively relaxed, centrally concentrated morphology. Images are 1 Mpc on a side. Middle row: zoomed-in optical images of the cluster core, showing the central BCG in each cluster. These images are made by combining the F606W (blue) and F814W (green, red) images from *HST* in such a way as to make the old stellar populations appear red and the young populations blue. Both SPT-CLJ0000-5748 and SPT-CLJ2331-5051 appear relatively quiescent in these colors, while SPT-CLJ2043-5035 and SPT-CLJ2344-4243 clearly have significant younger stellar components. Lower row: zoomed-in images showing the excess emission in the F606W band above the expectation for a passive stellar population, based on the F814W band image. These panels show an absence of emission for the quiescent (based on color) BCGs, and clumpy, extended emission for SPT-CLJ2043-5051 and SPT-CLJ2344-4243. This clumpy, blue emission, which is extended on scales of ~ 15 kpc (SPT-CLJ2043-5051) and $\gtrsim 50$ kpc (SPT-CLJ2344-4243), is further evidence for ongoing star formation.

massive companion that appears to be gas-poor, and may be in the midst of merging with the central galaxy, though this could be a projection effect. Both SPT-CLJ0000-5748 and SPT-CLJ2331-5051 have overall very red colors, and show no sign of structure in the F606W (rest-frame blue) band, indicating relatively old stellar populations and little to no star formation.

Both SPT-CLJ2043-5035 and SPT-CLJ2344-4243 harbor central galaxies with excess clumpy blue emission, indicating significant ongoing star formation. While these systems are similar in terms of their stellar populations, they are very different in other ways. SPT-CLJ2043-5035 has the largest BCG offset from the X-ray peak, while SPT-CLJ2344-4243 has no measurable offset between the X-ray peak and the central galaxy. The BCG in SPT-CLJ2043-5035 is the least massive at $M_* = 4.1 \times 10^{11} M_\odot$, while the BCG in SPT-CLJ2344-4243 is the most massive at $M_* = 14.5 \times 10^{11} M_\odot$. The blue emission in SPT-CLJ2043-5035 is extended on scales of ~ 15 kpc and appears to be double-peaked, while that in SPT-CLJ2344-4243 is centrally concentrated in a single peak

and extended on scales of $\gtrsim 50$ kpc. In both cases, the young stars may be the result of a gas-rich merger, and/or cooling of the low-entropy gas at the center of the cluster. It is challenging to differentiate between these two scenarios with the available data—the old stellar populations are not obviously disturbed in either system, but we also do not have a sufficiently red band with high enough angular resolution to definitely make such a statement. There is a potential donor galaxy to the east of the BCG in SPT-CLJ2043-5035, but it is quite small and symmetric—to lose enough gas to fuel such a large amount of star formation, it would have to be fully disrupted. We will discuss these systems further in Section 4.1.

In Figure 2, we showed the optical spectra of the four BCGs in this sample. These BCGs represent four very different phases of galaxy evolution. SPT-CLJ2043-5035 and SPT-CLJ2344-4243 both have strong [O II] emission and no evidence of a 4000 \AA break, indicating that the light is dominated by young stellar populations. The specific star formation rates (sSFR) of these systems are 0.09 Gyr^{-1} and

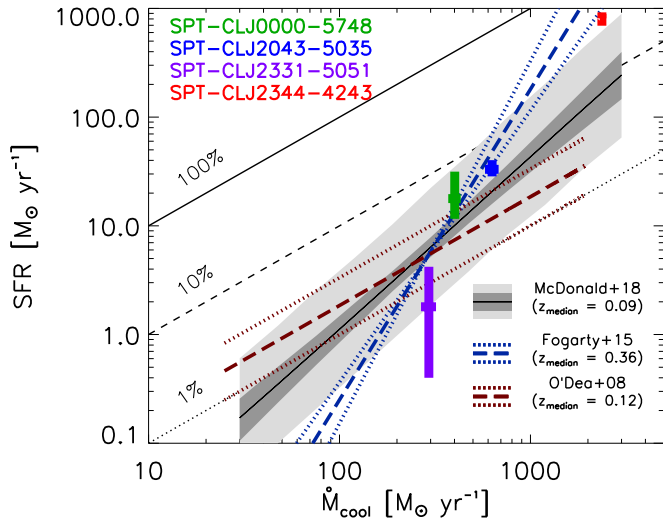


Figure 8. BCG star formation rate compared to classical cooling rate ($\dot{M}_{\text{cool}} \equiv \dot{M}_g(r < r_{\text{cool}})/t_{\text{cool}}$) for the four clusters in our sample. These star formation rates are based on the [O II] emission line, and are corrected for intrinsic extinction as measured from the CIGALE fit to the broadband SED. For comparison, we show the relations found in O’Dea et al. (2008, dark red) and McDonald et al. (2018, black/gray) for clusters at $z \sim 0.1$. For the latter, we show the uncertainty on the fit in dark gray, and the measured scatter in light gray. In blue, we show the fit to CLASH clusters from Fogarty et al. (2015), which are at considerably higher redshift. Overall, the relaxed clusters in the SPT sample (including Phoenix (McDonald et al. 2012), which is the most relaxed SPT-selected cluster) tend to host BCGs with higher SFR per unit cooling ICM than clusters at $z \sim 0$.

0.554 Gyr^{-1} , indicating that, while both are rapidly forming stars, this star formation is only contributing significantly to the growth of SPT-CLJ2344-4243, which will double its mass in $\sim 2 \text{ Gyr}$ (compared to $\sim 10 \text{ Gyr}$ for SPT-CLJ2043-5035). SPT-CLJ0000-5748 also has notable [O II] emission, but also exhibits a strong 4000 \AA break and deep absorption lines, indicative of an old stellar population dominating the emission. The corresponding sSFR for this system is 0.014 Gyr^{-1} , indicating that star formation is contributing negligibly to the growth of the total stellar mass. This is consistent with Figure 7, in which the light is dominated by the smooth, red stellar population. Finally, SPT-CLJ2331-5051 provides a fourth spectral type: no significant [O II] emission, and an overall old stellar population (strong 4000 \AA break, deep absorption lines). This BCG has an sSFR of 0.002 Gyr^{-1} , indicating that it is evolving almost completely passively.

Despite living in nearly identical clusters (see Figures 3, 4, 5), these four BCGs span a factor of ~ 500 in specific star formation rate. In Figure 8, we compare the cooling rate to the BCG star formation rate, following McDonald et al. (2018), where we are assuming that the star formation in the BCG is connected to the cooling of the hot ICM (we will address this assumption in Section 4.1). While the host clusters span a factor of < 10 in cooling rate, the BCGs span a factor of ~ 500 in star formation rate, consistent with the considerable scatter in star formation rates at fixed cooling rate measured in McDonald et al. (2018). These four systems are consistent with the trends found both by Fogarty et al. (2015) for clusters at $z \sim 0.4$ and by McDonald et al. (2018) for clusters at $z \sim 0.1$. Both of these studies find a slope greater than unity, suggesting that the more massive, strongly cooling clusters are also cooling more efficiently. For one out of the four clusters (SPT-CLJ2344-4243), the ratio of the star formation rate to the

cooling rate is outside the 1σ scatter measured for a sample of > 100 cool core clusters at $z \sim 0$ (McDonald et al. 2018), consistent with expectations. If the star formation in all of these systems can be attributed to cooling, it suggests that, with the exception of the Phoenix cluster (SPT-CLJ2344-4243), cooling is suppressed as effectively at early times as it is today. We will discuss this further in Section 4.1.

In summary, all four clusters host massive, central galaxies within $\lesssim 10 \text{ kpc}$ of the X-ray peak, consistent with low- z observations of relaxed clusters. These central galaxies span a range of stellar populations, from completely passive (SPT-CLJ2331-5051) to rapidly star-forming (SPT-CLJ2043-5035), to starburst (SPT-CLJ2344-4243), despite living at the centers of very similar clusters.

4. Discussion

4.1. What is the Origin of the Star Formation?

Figures 2 and 7 demonstrate that, despite sharing similar properties on the cluster scale, the central BCGs in these four clusters could not be more different, spanning the full range from passive to starburst. In the cases of SPT-CLJ2043-5035 and SPT-CLJ2344-4243, the star formation rates imply the presence of a tremendous amount of cold gas. This cold gas is most likely the result of either cooling of the hot ICM, so-called “residual cooling flows” (see, e.g., McDonald et al. 2018), or stripping of gas-rich galaxies as they pass through the dense cluster core. In this section we will attempt to differentiate between these two scenarios given the available data.

The morphology of the blue excess in SPT-CLJ2043-5035 (Figure 7) is more similar to that of a gas-rich merger than that of a typical cool core cluster. The extended blue emission points toward a smaller red galaxy to the east of the BCG, consistent with a scenario in which a satellite galaxy was stripped while passing close to the central BCG. However, such a double-peaked morphology in the blue excess could also be a result of a sloshing cool core. There are several low- z systems where the cool core has been “dislodged” from the BCG by a minor interaction, leading to the condensation of low-entropy gas away from the direct influence of the AGN (Hamer et al. 2012). In this case, a minor merger would be responsible for setting the core in motion, but the cool gas would originate in the hot phase, not in a donor galaxy. We will investigate further the relationship between the dynamical state of these clusters and the properties of the BCG and their AGN in a companion paper.

Conveniently, the north–south oriented long slit that was placed on the BCG captures much of the extended blue emission, as we show in Figure 9. The two-dimensional spectrum, shown in the right panel of Figure 9, shows extended [O II] emission, with a velocity gradient of $\sim 200 \text{ km s}^{-1}$ across the extended emission. For comparison, the velocity spread observed for stripped galaxies in dense environments from the Gas Stripping Phenomena (GASP) survey is significantly higher, with measured values of $\Delta v \sim 500 \text{ km s}^{-1}$ (J0201, J0206; Poggianti et al. 2017a, 2017b), consistent with the velocity dispersions measured in the host cluster. Given that the clusters considered here are more massive than those from the GASP survey, we would expect even higher velocity widths across the length of the stripped gas. However, if the stripping is happening in the plane of the sky, the velocity spread could be significantly diminished, to (or below) the

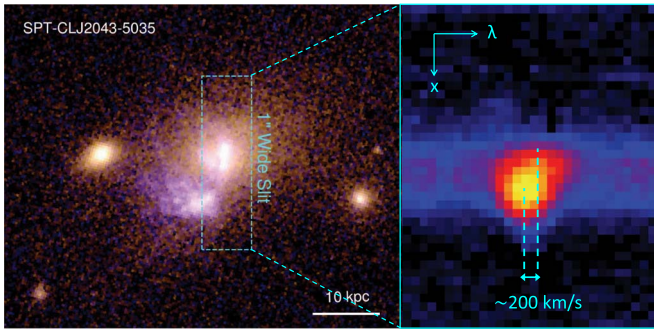


Figure 9. Left: pseudo-color image, combining the F606W and F814W filters on the *HST*, of the central galaxy in SPT-CLJ2043-5035. The cyan rectangle shows the position of the slit that was used to obtain the optical spectrum (Figure 2). Right: two-dimensional spectrum, extracted along the slit shown in the left panel, and centered on the [O II] $\lambda\lambda 3726, 3729$ doublet. This spectrum shows that the emission peak shifts by $\sim 200 \text{ km s}^{-1}$ over the extent of the extended line emission.

levels observed here. For comparison, the velocities spanned by cooling, multiphase gas in the cores of nearby clusters are $\sigma_v \sim 100\text{--}200 \text{ km s}^{-1}$ (e.g., Gaspari et al. 2018), fully consistent with what we observe in SPT-CLJ2043-5035.

Beyond the morphology and dynamics, we can consider the amount of star formation, and whether it could realistically be fueled by stripping. For SPT-CLJ2043-5035, the nearest galaxy (east of the BCG in Figure 9) is the most likely donor, and has a stellar mass $\sim 5\times$ smaller than the BCG, based on its *i*-band brightness. Combining the amount of star formation with the stellar mass of the donor galaxy yields a specific star formation rate of 0.4 Gyr^{-1} . For comparison, this is only slightly higher than for typical stripped dwarf galaxies in the GASP survey ($\text{sSFR} \sim 0.2\text{--}0.3 \text{ Gyr}^{-1}$; Vulcani et al. 2017; George et al. 2018), and much less than we see in starburst galaxies such as M82 and NGC 1569 ($\text{sSFR} \sim 1.0 \text{ Gyr}^{-1}$; Jarrett et al. 2017). For SPT-CLJ2344-4243, the implied sSFR in the nearest potential donor galaxy is $\sim 10 \text{ Gyr}^{-1}$, which is an order of magnitude higher than the most vigorous starbursts that we observe (e.g., Jarrett et al. 2017). As discussed in McDonald et al. (2012), this is strong evidence against the fueling of star formation by the stripping of infalling gas in this system, because it would require several (~ 10) gas-rich galaxies all simultaneously donating their gas.

Finally, there is evidence provided by the cooling properties of the ICM. The rank orders of the cooling rate and the star formation rate are identical—i.e., the strongest cool core harbors the most star-forming BCG, the second strongest cool core has the second most star-forming BCG, etc. If the star formation is unrelated to cooling, this would happen by chance $< 5\%$ of the time. Both SPT-CLJ2043-5035 and SPT-CLJ2344-4243, which harbor BCGs forming stars on large physical scales ($> 10 \text{ kpc}$), have entropy profiles that fall below the gravity-only prediction (Voit et al. 2005) between 30 and 100 kpc, while the other two clusters (which show no evidence of extended star formation) lie above it at all radii. The fact that both the entropy profiles and BCG stellar populations divide the four clusters into the same two groups suggests that the star formation is fed by the cooling ICM, though this is not conclusive.

Indeed, none of these arguments alone provides conclusive evidence for a cooling, rather than stripping, origin for the star-forming gas. While it seems most probable that SPT-CLJ2344-4243 is fed by cooling, based solely on the overwhelming

amount of available cold gas that would have to come from several donors, the picture is not so clear for SPT-CLJ2043-5035. The morphology appears to favor a stripping origin, while the thermodynamic profiles seem to favor cooling. The dynamics and total amount of star formation do not strongly favor either interpretation. With deeper X-ray data we could look for a spatial correlation between the low-entropy gas and the star formation, while deeper, ideally spatially resolved (i.e., IFU), optical spectroscopy could allow us to investigate the kinematics and metallicity of the young stars, and whether these are more similar to the cooling ICM or to the nearest donor galaxy.

4.2. Metal Enrichment in Cluster Cores

One of the leading explanations for the centrally peaked metallicity profile is that the BCG has enriched the ICM in the immediate vicinity via type Ia supernovae (SNe) over several gigayears (e.g., De Grandi et al. 2004). In such a scenario, we may expect a significant change in the magnitude of the central metallicity excess between $z \sim 0.7$ and $z \sim 0$, which represents 6 Gyr, or nearly half of the age of the universe. We can calculate the expected type Ia supernova rates (SNR) from the central galaxy between $z = 2$ (roughly the cluster formation time) and $z = 0.7$, and then $z = 0.7$ and $z = 0$, to estimate roughly what fraction of the central metallicity excess was formed at late times, if this is indeed the enrichment mechanism. We assume SNR from Perrett et al. (2012), which account for both prompt SNe shortly after the formation of massive stars (scaling with SFR), and delayed SNe, which occur much later (scaling with stellar mass):

$$\text{SNR}_{\text{Ia}}(z) = 1.9 \times 10^{-14} M_*(z) + 3.3 \times 10^{-4} \text{SFR}(z), \quad (5)$$

where we take the BCG stellar mass as a function of redshift from De Lucia et al. (2006), with $M_* = 5 \times 10^{11} M_\odot$ at $z = 0$, and the BCG star formation rate as a function of redshift from Bonaventura et al. (2017). We find that 24% of type Ia supernovae in BCGs should have exploded at $z < 0.7$, with the bulk of SNe Ia going off at earlier times. Assuming that both prompt and delayed SNe Ia enrich at the same rate, this would imply that only 24% of the metallicity peak was formed at $z < 0.7$. We note that this does not account for core-collapse SNe, which likely dominated at early times when BCGs were exceptionally star-forming (see McDonald et al. 2016a; Bonaventura et al. 2017). Thus, we expect this to represent an upper limit on the fraction of metals produced in cluster cores at $z < 0.7$ compared to $z > 0.7$. Given that the measurement uncertainty on the metallicity within 10 kpc is $\sim 25\%$, we are unable to confirm this increase of $< 24\%$ over the past 6 Gyr. Based on this simple Ia-only model, we expect $\sim 50\%$ of the core enrichment to happen between $z = 2$ and $z = 1.5$, and so it is unsurprising that we, and previous studies (e.g., Mantz et al. 2017), do not see a strong evolution in the central metallicity excess. To properly trace the growth of this central metallicity peak, we require larger samples of similar-quality data (to probe metallicity on $\sim 10 \text{ kpc}$ scales), spanning a larger range of redshift where the changes in metallicity should be more dramatic.

Perhaps more important in dictating the shape of the metallicity profile at late times ($z < 1$) is the central AGN. Kirkpatrick et al. (2011) showed that radio-loud AGNs in the

centers of clusters can push metals from the central core to large radii ($\gtrsim 100$ kpc). Figure 6 shows that all three clusters for which we can constrain the central metallicity have a metallicity peak in the inner ~ 10 kpc that is overenriched at the 1σ level when compared to the average profile for low-redshift cool core clusters from Baldi et al. (2007). If pushed to radii of 50–100 kpc (a volume thousands of times larger) these metals would quickly be diluted, and the metallicity profile would be indistinguishable from the profile of Baldi et al. (2007). Thus, the presence, or lack, of a sharply peaked metallicity profile may be telling us more about the amount of time elapsed since the last major outburst of AGN feedback than it is about the enrichment history of the cluster core. Given how centrally concentrated the metallicity profiles are in these three systems, it is likely that none of them has experienced a major outburst in a few hundred million years, which corresponds to the freefall time at a radius of ~ 100 kpc. This is corroborated by the fact that the observed bubbles in these systems are at relatively small radii, indicating ongoing, rather than past, feedback (Hlavacek-Larrondo et al. 2015). We will investigate this scenario further in a companion paper, focusing specifically on the feedback and dynamical properties of these four clusters.

5. Summary

We present new data from the *Chandra X-ray Observatory* and the *Hubble Space Telescope*, targeting the four most relaxed clusters in the initial SPT 2500 deg² survey. These represent some of the deepest data currently available for clusters at $z > 0.5$. In this work, we focus on the cooling properties of the ICM, along with the stellar populations of the central BCG. We find:

1. The thermodynamic profiles of all four clusters are very similar to one another and to clusters at $z \sim 0$. This includes the shape of the temperature profile, which is well described by the universal model (Vikhlinin et al. 2006), and the entropy profile, which is well described by the ensemble profiles for clusters at $z \sim 0$ (e.g., Walker et al. 2012; Panagoulia et al. 2014; Babyk et al. 2018). We find no evidence for deviations from self-similar evolution in the temperature profiles, implying that the process responsible for preventing runaway cooling over the past $\gtrsim 6$ Gyr is preserving self-similarity. We compare the measured thermodynamic profiles to those published in McDonald et al. (2013b)—based on data a factor of ~ 5 shallower—and find good agreement, suggesting that the assumptions made when interpreting data with low signal-to-noise ratio (e.g., shape of temperature profile, constant metallicity, fixed redshift) are valid for relaxed clusters.
2. Despite representing 6 Gyr in evolution between our sample and well-studied low- z clusters, we see no evidence for a change in the cooling properties of the core, with drops in central temperature of 0.15–0.4 (compared to typical values of 0.1–0.4 for cool core clusters at $z \sim 0$; Vikhlinin et al. 2006), central ($r \sim 5$ kpc) entropies of 11–16 keV cm² (compared to typical values of ~ 15 keV cm² for cool core clusters at $z \sim 0$; Panagoulia et al. 2014), and central cooling times of 0.18–0.32 Gyr (compared to typical values of 0.3–0.8 for cool core clusters at $z \sim 0$; Hogan et al. 2017). This implies a

tight balance between heating and cooling over the past ≥ 6 Gyr.


3. We find that the metallicity of the ICM in both the central region ($r < 0.1 R_{500}$) and core-excised region (0.1–0.5 R_{500}) agrees well with what is found at $z \sim 0$. This adds further evidence for early enrichment of the ICM. Interestingly, we find mild (1σ) evidence for over-enriched cores at $z \sim 0.7$ compared to $z \sim 0$. We calculate that the bulk ($> 76\%$) of metallicity excess observed at the centers of clusters today came from supernovae at $z > 0.7$, confirming that we should not expect to see a strong evolution in the central metal excess over the past 6 Gyr. We propose that, instead, the variations in central metallicity are telling us more about the timescales of strong AGN feedback (which can redistribute metals). This would imply that the three systems for which we constrain the inner metallicity here have not experienced a major AGN outburst, capable of pushing metals outside ~ 100 kpc, in the last few hundred million years.
4. Despite sharing remarkably similar cooling properties (e.g., central cooling time, classical cooling rate), the central galaxies in these four clusters exhibit markedly different stellar populations, ranging from completely passive (SPT-CLJ2331-5051: no emission lines, strong 4000 Å break), to weakly star-forming (SPT-CLJ0000-5748: weak emission lines, strong 4000 Å break), to strongly star-forming (SPT-CLJ2043-5035: strong emission lines, weak 4000 Å break), to starburst (SPT-CLJ2344-4244: young stellar populations dominate emission). If all of this star formation is due to cooling of the hot ICM (which may not be the case for SPT-CLJ2043-5035), it implies that the relationship between the cooling rate and star formation rate at early times is similar to that observed for nearby clusters, with considerable scatter in star formation at fixed cooling rate and a steeper-than-unity slope in the star formation rate as a function of cooling rate.

This analysis provides a reference point for our past and future analyses of distant clusters. Observations of such systems are, by necessity, typically shallow, requiring leaps of faith in interpreting unresolved ground-based data or low-count X-ray data. With these deep data of high angular resolution, we can anchor these analyses at the halfway point of cluster evolution, providing confidence when future observations extend these measurements even further into the past.

Support for this work was provided by NASA through *Chandra* Award Numbers GO6-17112A and GO6-17112B issued by the *Chandra X-ray Observatory Center*, which is operated by the Smithsonian Astrophysical Observatory for and on behalf of the National Aeronautics & Space Administration under contract NAS8-03060. Additional support was provided by NASA through grants from the Space Telescope Science Institute (HST-GO-13578, HST-GO-14352), which is operated by the Association of Universities for Research in Astronomy, Incorporated, under NASA contract NAS5-26555. The South Pole Telescope is supported by the National Science Foundation through grant PLR-1248097. Partial support is also provided by the NSF Physics Frontier Center grant PHY-1125897 to the Kavli Institute of Cosmological Physics at the University of Chicago, the Kavli Foundation and the Gordon

and Betty Moore Foundation grant GBMF 947. S.W.A. and A.B.M. acknowledge additional support from the U.S. Department of Energy under contract number DE-AC02-76SF00515. J.H.L. is supported by NSERC through the discovery grant and Canada Research Chair programs. W.F. acknowledges support from NASA contract NAS-08060 and the Smithsonian Institution. The Munich group acknowledges the support by the DFG Cluster of Excellence “Origin and Structure of the Universe”, the Ludwig-Maximilians-Universität (LMU-Munich), and the Transregio program TR33 “The Dark Universe.” T.S. acknowledges support from the German Federal Ministry of Economics and Technology (BMW) provided through DLR under projects 50 OR 1210, 50 OR 1407, and 50 OR 1610. The Melbourne group acknowledges support from the Australian Research Council’s Discovery Projects funding scheme (DP150103208). B.B. is supported by the Fermi Research Alliance, LLC under Contract No. DE-AC02-07CH11359 with the U.S. Department of Energy.

ORCID iDs

J. Hlavacek-Larrondo  <https://orcid.org/0000-0001-7271-7340>
M. Bayliss  <https://orcid.org/0000-0003-1074-4807>
M. Brodwin  <https://orcid.org/0000-0002-4208-798X>
W. R. Forman  <https://orcid.org/0000-0002-9478-1682>
G. P. Garmire  <https://orcid.org/0000-0002-7371-5416>
G. Khullar  <https://orcid.org/0000-0002-3475-7648>
C. L. Reichardt  <https://orcid.org/0000-0003-2226-9169>

References

- Anders, E., & Grevesse, N. 1989, *GeCoA*, **53**, 197
- Appenzeller, I., Fricke, K., Fürtig, W., et al. 1998, *Msngr*, **94**, 1
- Arnaud, K. A. 1996, in ASP Conf. Ser. 101, *Astronomical Data Analysis and Systems V*, ed. G. H. Jacoby & J. Barnes (San Francisco, CA: ASP), 17
- Asplund, M., Grevesse, N., Sauval, A. J., & Scott, P. 2009, *ARA&A*, **47**, 481
- Babik, I. V., McNamara, B. R., Nulsen, P. E. J., et al. 2018, *ApJ*, **862**, 39
- Baldi, A., Ettori, S., Mazzotta, P., Tozzi, P., & Borgani, S. 2007, *ApJ*, **666**, 835
- Baldi, A., Ettori, S., Molendi, S., et al. 2012a, *A&A*, **537**, A142
- Baldi, A., Ettori, S., Molendi, S., & Gastaldello, F. 2012b, *A&A*, **545**, A41
- Bayliss, M. B., Ruel, J., Stubbs, C. W., et al. 2016, *ApJS*, **227**, 3
- Bleem, L. E., Stalder, B., de Haan, T., et al. 2015, *ApJS*, **216**, 27
- Bonaventura, N. R., Webb, T. M. A., Muzzin, A., et al. 2017, *MNRAS*, **469**, 1259
- Buote, D. A., & Tsai, J. C. 1995, *ApJ*, **452**, 522
- Burgarella, D., Buat, V., & Iglesias-Páramo, J. 2005, *MNRAS*, **360**, 1413
- Calzetti, D., Kinney, A. L., & Storchi-Bergmann, T. 1994, *ApJ*, **429**, 582
- Carlberg, R. G., Yee, H. K. C., Ellingson, E., et al. 1997, *ApJL*, **476**, L7
- Cavagnolo, K. W., Donahue, M., Voit, G. M., & Sun, M. 2008, *ApJL*, **683**, L107
- Cavagnolo, K. W., Donahue, M., Voit, G. M., & Sun, M. 2009, *ApJS*, **182**, 12
- Chiu, I., Mohr, J. J., McDonald, M., et al. 2016, *MNRAS*, **455**, 258
- Chiu, I., Mohr, J. J., McDonald, M., et al. 2018, *MNRAS*, **478**, 3072
- Dale, D. A., Helou, G., Magdis, G. E., et al. 2014, *ApJ*, **784**, 83
- De Grandi, S., Ettori, S., Longhetti, M., & Molendi, S. 2004, *A&A*, **419**, 7
- De Grandi, S., & Molendi, S. 2001, *ApJ*, **551**, 153
- De Lucia, G., Springel, V., White, S. D. M., Croton, D., & Kauffmann, G. 2006, *MNRAS*, **366**, 499
- Dressler, A., Bigelow, B., Hare, T., et al. 2011, *PASP*, **123**, 288
- Dunn, R. J. H., & Fabian, A. C. 2006, *MNRAS*, **373**, 959
- Ettori, S., Baldi, A., Balestra, I., et al. 2015, *A&A*, **578**, A46
- Ezer, C., Bulbul, E., Nihal Ercan, E., et al. 2017, *ApJ*, **836**, 110
- Fogarty, K., Postman, M., Connor, T., Donahue, M., & Moustakas, J. 2015, *ApJ*, **813**, 117
- Gaspari, M., McDonald, M., Hamer, S. L., et al. 2018, *ApJ*, **854**, 167
- George, K., Poggianti, B. M., Gullieuszik, M., et al. 2018, *MNRAS*, **479**, 4126
- Haarsma, D. B., Leisman, L., Donahue, M., et al. 2010, *ApJ*, **713**, 1037
- Hamer, S. L., Edge, A. C., Swinbank, A. M., et al. 2012, *MNRAS*, **421**, 3409
- Hlavacek-Larrondo, J., Fabian, A. C., Edge, A. C., et al. 2012, *MNRAS*, **421**, 1360
- Hlavacek-Larrondo, J., McDonald, M., Benson, B. A., et al. 2015, *ApJ*, **805**, 35
- Hogan, M. T., McNamara, B. R., Pulido, F. A., et al. 2017, *ApJ*, **851**, 66
- Hook, I. M., Jørgensen, I., Allington-Smith, J. R., et al. 2004, *PASP*, **116**, 425
- Jarrett, T. H., Cluver, M. E., Magoulas, C., et al. 2017, *ApJ*, **836**, 182
- Jeltema, T. E., Canizares, C. R., Bautz, M. W., & Buote, D. A. 2005, *ApJ*, **624**, 606
- Kaiser, N. 1986, *MNRAS*, **222**, 323
- Kewley, L. J., Geller, M. J., & Jansen, R. A. 2004, *AJ*, **127**, 2002
- Kirkpatrick, C. C., McNamara, B. R., & Cavagnolo, K. W. 2011, *ApJL*, **731**, L23
- Koekemoer, A. M., Fruchter, A. S., Hook, R. N., & Hack, W. 2003, in HST Calibration Workshop: Hubble after the Installation of the ACS and the NICMOS Cooling System, ed. S. Arribas, A. Koekemoer, & B. Whitmore (Baltimore, MD: Space Telescope Science Institute), 337
- Leccardi, A., & Molendi, S. 2008, *A&A*, **487**, 461
- Mantz, A. B., Allen, S. W., Morris, R. G., et al. 2015, *MNRAS*, **449**, 199
- Mantz, A. B., Allen, S. W., Morris, R. G., et al. 2017, *MNRAS*, **472**, 2877
- Mantz, A. B., Allen, S. W., Morris, R. G., & Schmidt, R. W. 2016, *MNRAS*, **456**, 4020
- Massey, R., Schrabback, T., Cordes, O., et al. 2014, *MNRAS*, **439**, 887
- McDonald, M., Allen, S. W., Bayliss, M., et al. 2017, *ApJ*, **843**, 28
- McDonald, M., Bayliss, M., Benson, B. A., et al. 2012, *Natur*, **488**, 349
- McDonald, M., Benson, B., Veilleux, S., Bautz, M. W., & Reichardt, C. L. 2013a, *ApJL*, **765**, L37
- McDonald, M., Benson, B. A., Vikhlinin, A., et al. 2013b, *ApJ*, **774**, 23
- McDonald, M., Benson, B. A., Vikhlinin, A., et al. 2014a, *ApJ*, **794**, 67
- McDonald, M., Bulbul, E., de Haan, T., et al. 2016b, *ApJ*, **826**, 124
- McDonald, M., Gaspari, M., McNamara, B. R., & Tremblay, G. R. 2018, *ApJ*, **858**, 45
- McDonald, M., McNamara, B. R., van Weeren, R. J., et al. 2015, *ApJ*, **811**, 111
- McDonald, M., Stalder, B., Bayliss, M., et al. 2016a, *ApJ*, **817**, 86
- McDonald, M., Swinbank, M., Edge, A. C., et al. 2014b, *ApJ*, **784**, 18
- McNamara, B. R., & O’Connell, R. W. 1989, *AJ*, **98**, 2018
- Mernier, F., de Plaa, J., Kaastra, J. S., et al. 2017, *A&A*, **603**, A80
- Mernier, F., de Plaa, J., Pinto, C., et al. 2016, *A&A*, **592**, A157
- Mohr, J. J., Evrard, A. E., Fabricant, D. G., & Geller, M. J. 1995, *ApJ*, **447**, 8
- Mohr, J. J., Fabricant, D. G., & Geller, M. J. 1993, *ApJ*, **413**, 492
- Nurgaliev, D., McDonald, M., Benson, B. A., et al. 2013, *ApJ*, **779**, 112
- Nurgaliev, D., McDonald, M., Benson, B. A., et al. 2017, *ApJ*, **841**, 5
- O’Dea, C. P., Baum, S. A., Privon, G., et al. 2008, *ApJ*, **681**, 1035
- Old, L., Wojtak, R., Pearce, F. R., et al. 2018, *MNRAS*, **475**, 853
- Panagoulia, E. K., Fabian, A. C., & Sanders, J. S. 2014, *MNRAS*, **438**, 2341
- Perrett, K., Sullivan, M., Conley, A., et al. 2012, *AJ*, **144**, 59
- Poggianti, B. M., Gullieuszik, M., Moretti, A., et al. 2017b, *Msngr*, **170**, 29
- Poggianti, B. M., Moretti, A., Gullieuszik, M., et al. 2017a, *ApJ*, **844**, 48
- Rasia, E., Meneghetti, M., & Ettori, S. 2013, *AstRv*, **8**, 40
- Rossetti, M., Gastaldello, F., Ferioli, G., et al. 2016, *MNRAS*, **457**, 4515
- Ruel, J., Bazin, G., Bayliss, M., et al. 2014, *ApJ*, **792**, 45
- Runge, J., & Yan, H. 2018, *ApJ*, **853**, 47
- Salpeter, E. E. 1955, *ApJ*, **121**, 161
- Sanderson, A. J. R., O’Sullivan, E., & Ponman, T. J. 2009, *MNRAS*, **395**, 764
- Santos, J. S., Rosati, P., Tozzi, P., et al. 2008, *A&A*, **483**, 35
- Schmidt, R. W., Fabian, A. C., & Sanders, J. S. 2002, *MNRAS*, **337**, 71
- Schrabback, T., Applegate, D., Dietrich, J. P., et al. 2018, *MNRAS*, **474**, 2635
- Schrabback, T., Hartlap, J., Joachimi, B., et al. 2010, *A&A*, **516**, A63
- Semler, D. R., Šuhada, R., Aird, K. A., et al. 2012, *ApJ*, **761**, 183
- Sun, M. 2009, *ApJ*, **704**, 1586
- Sunyaev, R. A., & Zeldovich, Y. B. 1972, *CoASP*, **4**, 173
- Ueda, S., Hayashida, K., Anabuki, N., et al. 2013, *ApJ*, **778**, 33
- Vikhlinin, A. 2006, *ApJ*, **640**, 710
- Vikhlinin, A., Burenin, R., Forman, W. R., et al. 2007, in *Heating versus Cooling in Galaxies and Clusters of Galaxies*, ed. H. Böhringer et al. (Berlin: Springer), 48
- Vikhlinin, A., Burenin, R. A., Ebeling, H., et al. 2009, *ApJ*, **692**, 1033
- Vikhlinin, A., Kravtsov, A., Forman, W., et al. 2006, *ApJ*, **640**, 691
- Vikhlinin, A., McNamara, B. R., Forman, W., et al. 1998, *ApJL*, **498**, L21
- Voit, G. M., Kay, S. T., & Bryan, G. L. 2005, *MNRAS*, **364**, 909
- Vulcani, B., Moretti, A., Poggianti, B. M., et al. 2017, *ApJ*, **850**, 163
- Walker, S. A., Fabian, A. C., Sanders, J. S., & George, M. R. 2012, *MNRAS*, **427**, L45
- Webb, T. M. A., Muzzin, A., Noble, A., et al. 2015, *ApJ*, **814**, 96
- Wen, Z. L., & Han, J. L. 2013, *MNRAS*, **436**, 275
- Werner, N., Urban, O., Simionescu, A., & Allen, S. W. 2013, *Natur*, **502**, 656